Korean J. Chem. Eng., 36(5), 701-712 (2019)
DOI: 10.1007/s11814-019-0260-8

pISSN: 0256-1115
eISSN: 1975-7220

Synthesis of phosphate functionalized highly porous activated carbon and its utilization as an efficient copper (II) adsorbent

Somen Mondal† and Subrata Kumar Majumder†

Department of Chemical Engineering, Indian Institute of Technology Guwahati, Guwahati 781039, India
(*Received 25 January 2019 • accepted 27 March 2019*)

Abstract−The effects of activating agents on the characteristics of the activated carbons prepared from the tea waste were investigated. A three-step chemical activation process consisting of impregnation, carbonization and the secondary activation or phosphate functionalization was followed for the synthesis of the activated carbons. The surface area and the total pore volume of the best-activated carbon prepared in the present investigation at optimized conditions were found to be 1,329 m^2/g and 0.4167 cm^3/g. The potentiality of the copper adsorption onto the best quality activated carbon with the highest surface area and pore volume was investigated. The maximum adsorption capacity of the activated carbon was 76.22 mg/gat room temperature (28 °C). The copper (II) adsorption onto the activated carbon followed the pseudo-second-order kinetics which satisfied the Langmuir and Dubinin-Radushkevich (D-R) adsorption isotherms. Best activated carbon obtained from the present investigation may be recommended to use in water purification processes as a revamped copper (II) bio-adsorbent.

Keywords: Activated Carbon, Phosphate Functionalization, Copper (II) Adsorption, Adsorption Kinetics, Characterization

INTRODUCTION

Activated carbon (AC) as an adsorbent is widely used in water purification and industrial wastewater treatment. The adsorption capacities of the AC are highly dependent on the pore volume and the specific surface area, which are related to the chemical properties of the precursor material, activating agent and the heat energy along with the heating rate employed in the activation process. Tea waste was considered as the precursor by the researchers for the utilization of the waste in our benefits as high surface area ACs can be made from it. Different activating agents like H_3PO_4 [1-8], NaOH [9,10], KOH [11-14], $ZnCl_2$ [8,15,16], CH_3COOK [17], H_2SO_4 [18], HNO_3 [3], K_2CO_3 [8], HCl [19] and boric acid [20] have been used so far by the researchers to get the high surface area ACs instead of changing the precursor. H_3PO_4 was used as the activating agent by previous researchers and in the present study also for its important role in the activation process: (a) it can act as an acid catalyst assisting the bond cleavage and formation reactions; (b) after the dehydration process it can act as an oxidant; and (c) it can also be connected with the substrate forming the C-O-P bond. The researchers used their ACs mainly for the removal of dyes (Methylene blue [3,21-24], Eosin yellow [21], Rhodamine B, Brilliant green, Crystal violet and orange G [5], Acid blue 25 and Acid blue 29 [17,19], Cibacron yellow [11], Reactive Green 19 and Reactive violet 5 [25], Basic violet [26], Malachite green [27]) and phenolic [3,7,28], or pharmaceutical compound removal as like Aspirin [8], p-Nitrophenol [1], Oxytetracycline [6], Sulfamethazine [29], Acetaminophen [30], Carbofuran [27], Ciprofloxacin [31]. Very few studies are available in literature for the adsorption of Cr^{+3} and Cr^{+6} [toxic metals] [18,32,33] ions onto the ACs prepared from the tea waste. ACs prepared from the tea waste and their activation processes, utilities and the surface area generated as shown in Table S1. According to the World Health Organization (WHO), copper is a toxic water pollutant beyond a certain limit. So, removal of copper from contaminated water is essential for environmental benefits. Development of a new economic activation process to produce the high surface area and good quality ACs for the efficient removal of Cu^{2+} from the contaminated water is a challenge in the present day scenario. The ACs prepared from various natural sources (sewage sludge-based AC [34], hazelnut shell AC [35,40], cassava peel AC [36], Tunisian date stones AC [37], grape bagasse AC [38], periwinkle shells AC [39], rubber wood sawdust AC [41], peanut hull AC [42], coirpith AC [43], ceibapentandra hulls AC [44]) rather than the tea waste-based ACs have been utilized for the copper (II) adsorption at the pH values of mainly 5 or 6 (Table 1). The peanut hull AC showed the highest copper (II) adsorption capacity of 65.60 mg/g so far. According to previous researchers, the Cu^{2+} adsorption onto the ACs followed the pseudo-second order kinetics along with the Langmuir isotherm model. In the present study, for the first time, the tea waste based AC has been utilized as Cu^{2+} adsorbent at the basic range of pH 9.46 (Table 1).

The novelty of the present work is to produce ACs from tea waste (used as a precursor material as it can provide higher surface area according to the previous literature) by a newly developed activation process to successfully remove the copper from contaminated water. The aforementioned work has not been reported in the literature yet to the best of our knowledge.

The present study also investigated the effect of operating parameters on the generation of pore volume and effective surface area of the ACs. The synthesis and characterization of the ACs are demon-

†To whom correspondence should be addressed.
E-mail: somen.mondal@iitg.ac.in, skmaju@iitg.ac.in

Table 1. Comparison of Cu (II) adsorption results of tea waste based AC with the other adsorbents

Adsorbents	pH	Q_m (mg/g)	Fitted isotherm model	Fitted kinetic model	Reference
Sewage sludge-based AC	5	7.73	Langmuir	Pseudo-second order	[34]
Hazelnut shell AC	6	58.27	Langmuir	Pseudo-second order	[35]
Cassava peel AC	5	56.17	Langmuir	-	[36]
Tunisian date stones AC	5	31.25	Langmuir	Pseudo-second order	[37]
Grape bagasse AC	5	43.47	Langmuir, D-R	Pseudo-second order	[38]
periwinkle shells AC	8	-	Langmuir, Freundlich	Pseudo-second order	[39]
Hazelnut shell AC	-	39.54	Langmuir	Pseudo-second order	[40]
Rubber wood sawdust AC	6	5.73	Langmuir	Pseudo-second order	[41]
Peanut hull AC	6	65.60	Langmuir	-	[42]
Coirpith AC	5	39.70	Langmuir, Freundlich	-	[43]
Ceibapentandra hulls AC	6	20.80	Langmuir, Freundlich	Pseudo-second order	[44]
Tea waste AC	9.46	76.22	Langmuir, D-R	Pseudo-second order	Present study

strated well in the present work. The adsorption kinetics and isotherms onto the best surface area AC are enunciated in the present study. Probably, the AC prepared from the tea waste exhibited the best adsorption capacity towards the copper (II) metal ions (76.22 mg/g) so far.

MATERIALS AND METHODS

ACs were prepared from the tea waste following a three-step chemical activation process. The tea wastes were washed with milli-Q water (Millipore Water Synthesis Unit, Model: Elix-3, Milli-Q; Make: Millipore, USA) thoroughly and oven dried at 95 °C for 48 hours. In the first step the dried sample was impregnated for 16-18 hours with the activating agents: either 50% diluted (vol%) H_3PO_4 (85%) or 50% $ZnCl_2$ (solid) solution (wt%) at a precursor to reagent ratio of 1 : 4 (wt%). The impregnated sample was transferred to the silica crucible and pyrolyzed at 500 °C for 1 hour at the heating rate of 10, 20 and 30 °C/min in a muffle furnace (Make: Ikon instruments, Model: IKO-011) in air atmosphere. The carbon samples were designated as X10, 20 and 30, respectively. The pyrolyzed sample was then activated again in the pure H_3PO_4 (85%) (X=H), a 50% mixture of H_3PO_4 (85%) and H_2SO_4 (98%) (X=HS), a saturated solution of $ZnCl_2$ (X=Zn), respectively, in the third and final step. The temperature for the pyrolysis of the raw material was selected based on the thermo-gravimetric analysis done by the Thermo Gravimetric Analyzer (TGA) (Model: TG 209 F1 Libra; Make: Netzsch, Germany). The ACs prepared from the tea waste were then washed with the milli-Q water and dried in hot air oven for 24 hours and preserved for further analysis (Fig. 1). The particle sizes of all the crushed AC samples used in the present study were in the range of 150 to 250 μm with an average of 200 μm (0.20 mm) measured by the screening sieves of sizes ASTM No. 60 and 100 (U.S. Standard).

The specific surface area and porosity of the ACs derived from the tea waste at different operating conditions were determined by N_2 adsorption at 77.3 K using the Brunauer-Emmett-Teller (BET) surface area analyzer (Model: Tristar II, Make: Micromeritics, U.S.A.) in the relative pressure range 0.01-1.0. The oven dried samples were degassed at 150 °C for 3 hours under vacuum before the BET measurements.

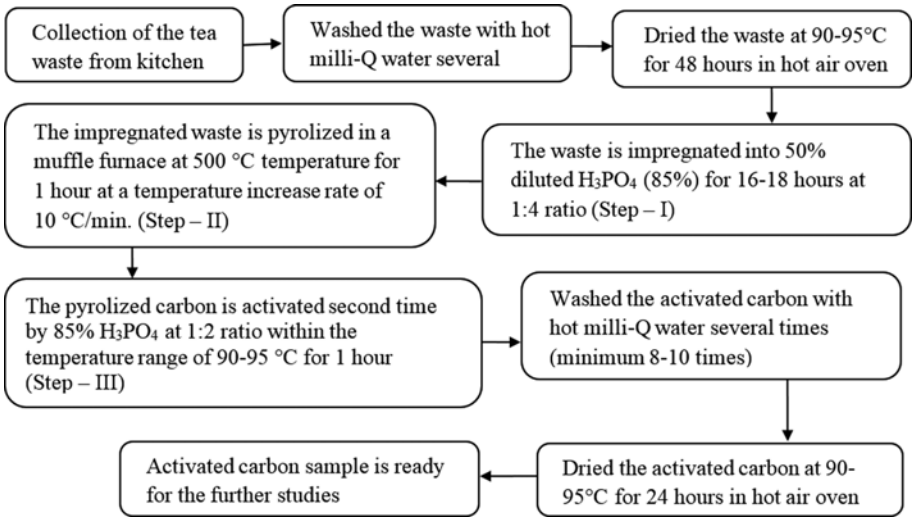

Fig. 1. Flow diagram of the best AC obtained from the tea waste following the three-step chemical activation process.

The surface functional groups of the ACs were recognized by transmission infrared spectra scattered from a Fourier transform spectrophotometer (Model: IRAffinity-1, Make: Shimadzu, Japan) using finely ground KBr containing about 0.5% of AC samples. The spectrograms were the average of 30 scans in each case with the wavelengths ranges from 400-4,000 cm^{-1}.

A laser micro Raman system (Make: Horiba Jobin Vyon, Model LabRam HR) was used to identify the graphitic nature of the produced carbon from the G, D and 2D band shift by scattering a monochromatic light of wavelength 488 nm.

The surface morphology of the best surface area AC prepared from the tea waste was examined with the field emission scanning electron microscope (FESEM) (Make: Zeiss, Model: Sigma, Germany). The compositions of the best AC before and after the copper adsorption were analyzed by energy-dispersive X-ray spectroscopy (EDS) in the FE-SEM machine. Total ash content in the AC was determined by burning the sample in the muffle furnace at 800 °C for 5 hours.

1. Adsorption Analysis

The copper (II) adsorption experiments on the derived AC were performed with laboratory grade $CuSO_4$, $5H_2O$ (copper sulfate pentahydrate) solutions of various concentrations (40-100 mg/*l*). The concentrations of Cu^{2+} in the initial and final solutions were estimated by using an atomic absorption spectrophotometer (AAS) (Model No.: Spectra AA 220 FS; Make: M/s Varian, Netherland). Batch equilibrium technique was used to determine the Cu^{2+} adsorption capacity on the prepared AC. The impacts of the contact time and the initial pH at the room temperature (27-28 °C) on the AC for the Cu^{2+} adsorption were investigated using the same technique.

2. Impact of the Initial pH on Adsorption

The impact of the initial pH on the adsorption capacities was investigated by adding 0.05 g AC samples in each case to 50 ml of $CuSO_4$, $5H_2O$ solution having the copper (II) concentration of 100 mg/*l* at initial pH values of 2.42, 5.08 and 9.46. The pH of the samples was measured by a table top pH meter (Equiptronics, EQ 610 model), and it was maintained with the addition of 0.1 (N) hydro-

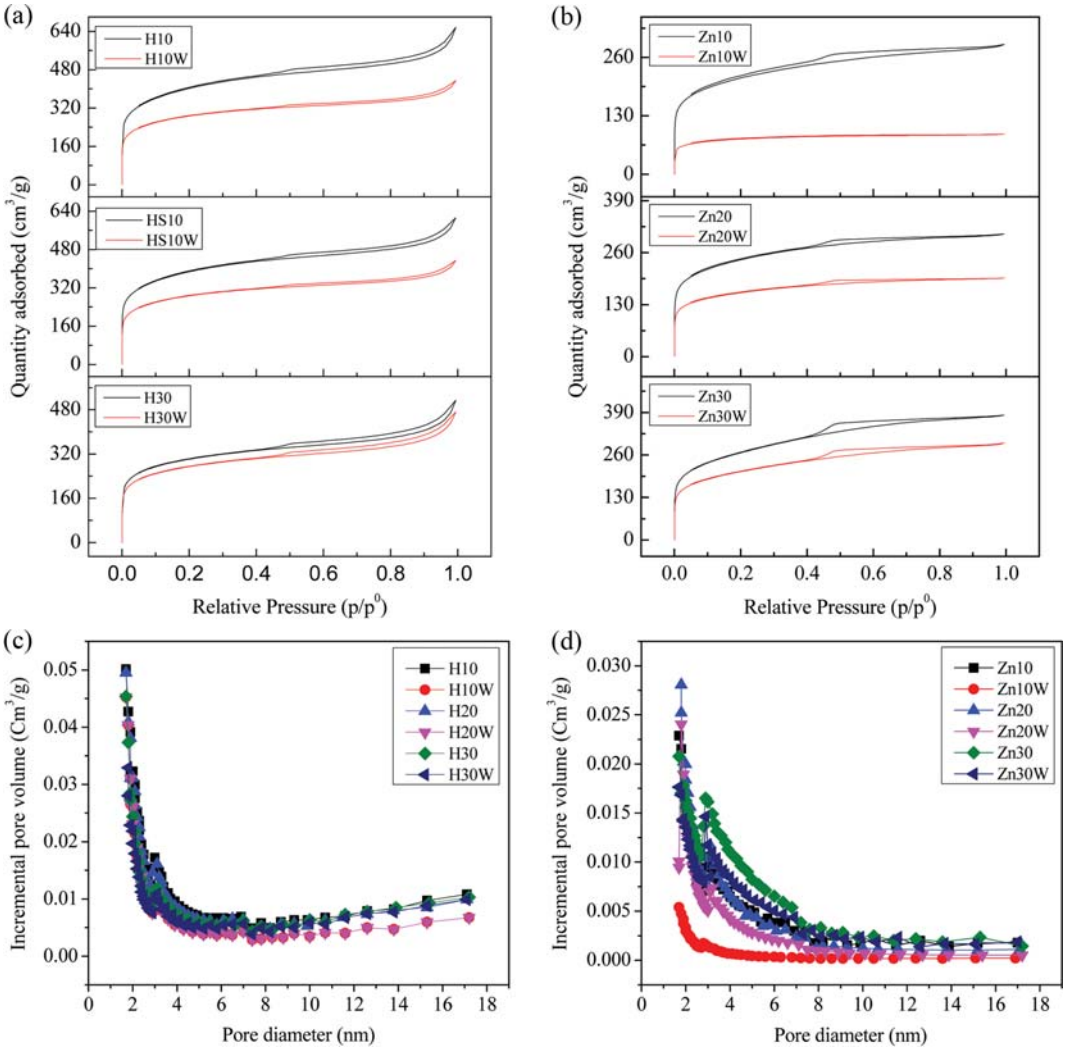

Fig. 2. (a) N_2 adsorption-desorption isotherms of the ACs H10, H10W, HS10, HS10W, H30, H30W; (b) N_2 adsorption-desorption isotherms of the ACs Zn10, Zn10W, Zn20, Zn20W, Zn30, Zn30W; (c) BJH pore size distribution curves of H10, H10W, HS10, HS10W, H30, H30W; and (d) BJH pore size distribution curves of Zn10, Zn10W, Zn20, Zn20W, Zn30, Zn30W.

Table 2. The BET and Langmuir surface area, pore distribution and average micropore diameters of the synthesized ACs

Activating agent	Carbonization heating rate (°C/min)	Pore volume (cm^3/g)					BET adsorption average pore diameter (nm)		BET surface area (m^2/g)		Langmuir surface area (m^2/g)	
		Micropore		Mesopore		Total pore						
		After pyrolysis	After second activation	After pyrolysis	After second activation	After second activation	After pyrolysis	After second activation	After pyrolysis	After second activation	After pyrolysis	After second activation
H_3PO_4	10	0.2090	0.2570	0.0940	0.1597	0.4167	1.2926	1.2543	937.71 ±12.90	1329.05 ±16.64	1487.56 ±10.45	2,146.57 ±18.18
H_3PO_4	30	0.2019	0.2289	0.0876	0.0921	0.3210	1.2902	1.3057	897.43 ±11.83	983.75 ±13.13	1448.51 ±12.39	1585.07 ±13.35
H_3PO_4+ H_2SO_4	10	0.2090	0.2572	0.0940	0.1467	0.4039	1.2926	1.2662	937.71 ±12.90	1275.79 ±16.32	1487.56 ±10.45	2050.43 ±16.55
$ZnCl_2$	10	0.0744	0.1346	0.0143	0.0865	0.2211	1.4158	1.2453	250.66 ±3.96	710.07 ±8.31	381.24 ±1.38	1,176.01 ±12.49
$ZnCl_2$	20	0.1203	0.1648	0.0532	0.0911	0.2559	1.3290	1.2816	522.23 ±6.75	798.52 ±9.74	838.37 ±6.68	1297.4 ±11.55
$ZnCl_2$	30	0.1099	0.1201	0.1035	0.1451	0.2652	1.2149	1.1714	702.66 ±6.95	905.54 ±8.21	1209.25 ±16.93	1583.96 ±24.27

chloric acid (HCl) and 5% ammonium hydroxide (NH_4OH) solutions to the initial solution of pH 5.08.

3. Equilibrium Kinetics and the Adsorption Studies

Batch experiments were carried out by taking 0.05 g of AC into 50 ml copper (II) solutions (100 mg/*l*) in 100 ml glass beakers at the room temperature. The persisting concentrations of the copper (II) ions in the solutions after the adsorption were tested by taking the filtrates at each time interval, and the adsorption capacities of the AC towards the copper (II) adsorption were calculated accordingly by subtracting the initial and final values of the concentrations ($Q_m = \frac{V}{m}(C_0 - C_e)$; where Q_m is the maximum adsorption capacity (mg/*l*), C_0 and C_e are the initial and final copper ion concentration (mg/*l*), V is the volume of water sample (*l*) and m is the mass of the adsorbent (g)). Each adsorption experiment was performed at least three times and the average values were reported. The obtained adsorption capacities (q_e and q_t) deviated (standard deviation) a maximum of 0.86 mg/g for pH 9.46 as shown in Fig. 8. Standard deviations are represented by error bars in Fig. 8, Fig. 9 and Fig. 10.

RESULTS AND DISCUSSION

1. Material Characteristics

The specific surface area and porosity of the ACs after pyrolysis and after the second activation with different activating agents at different heating rates were examined according to the N_2 adsorption-desorption isotherms as shown in Fig. 2.

The initial qualitative statistics on the adsorption process along with the pore-structure of the ACs can be made on the basis of the adsorption isotherms. As shown in Fig. 2(a), the ACs H10, H10W, HS10, HS10W, H30 and H30W impregnated with 50% diluted H_3PO_4 showed type-IV adsorption-desorption isotherms and type-H3 hysteresis loops specifying the highly porous structure with the higher specific surface area. A sharp increase in the profile at low relative pressure ($P/P^0<0.1$) indicates the existence of a significant amount of micropores and a noticeable hysteresis at higher relative pressure ($P/P^0=0.4$-1.0), indicating the existence of the large number of mesopores in the prepared AC samples [45]. Fig. 2(b) shows that the ACs activated with 50% $ZnCl_2$ solution (Zn10, Zn10W, Zn20, Zn20W, Zn30 and Zn30W) exhibited a type-I isotherm and H4 type hysteresis loop. At higher relative pressures, the almost horizontal nature of the isotherms signifies the microporous materials [46]. This will increase the adsorption at low relative pressures due to the increase of the interaction energy of the solid surfaces with the gas molecules [47]. The BET and Langmuir surface area of the ACs along with their pore distribution and average micropore diameters are shown in Table 2. The pore volume decreased with the increase of heating rate in case of acids (H_3PO_4 or H_3PO_4+H_2SO_4), but the generation of pore volume showed the opposite trend in case of acidic salt ($ZnCl_2$) activation due to the different reaction mechanisms followed by them. At a lower heating rate 10 °C/min, the H10 acquired the highest pore volume than the others. The same observation can be established from the BJH (Barrett-Joyner-Halenda) curves [48,49]. The BJH pore-size distribution curves of the prepared ACs are shown in Fig. 2(c) (for H10, H10W, HS10, HS10W, H30 and H30W) and Fig. 2(d) (for Zn10, Zn10W, Zn20, Zn20W, Zn30 and Zn30W). Narrow pore size distributions were observed for the prepared carbon samples within the range of 2.80-3.40 nm in case of acid activation and 2.70-4.10 nm in case of acidic salt activation. With the decrease of heating rate, the pore size distribution range increases for the samples H10, H20, H30, but the range decreases for the samples Zn10, Zn20, Zn30, which satisfied the results obtained from the N_2 adsorption-desorption data.

It clearly indicates that the AC prepared using H_3PO_4 at the heating rate of 10 °C/min. acquired the highest BET surface area (1,329 m^2/g) with the highest mesopore volume (0.1597 cm^3/g) (H10), and in each case, after the second activation, both the properties were improved, which explores the necessity of the subsequent activation or phosphate functionalization (Table 2).

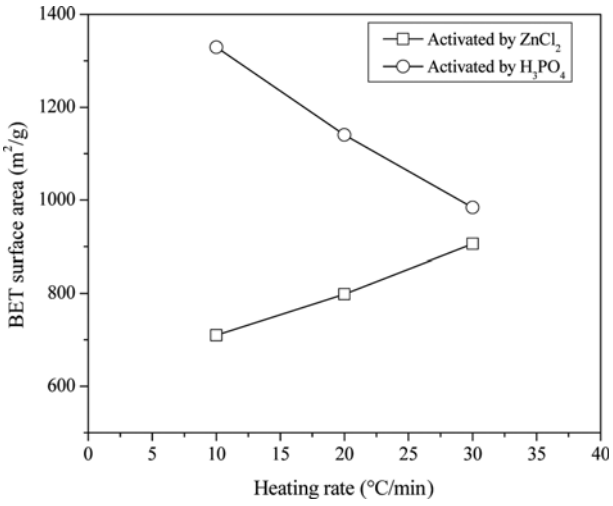

Fig. 3. Variation of the specific surface area with the heating rate.

The effect of heating rate on the BET surface area generation for a particular activating agent at the constant impregnation ratio (1 : 4, wt%) and the maximum carbonization temperature (500 °C) are shown in Fig. 3. The two activating agents (50% H_3PO_4 and 50% $ZnCl_2$) showed the opposite trends with the increase of the heating rate when the other operating variables were fixed. Initially, the moisture and small amount of volatiles were lost from the precursor. Then the volatile components and gasses were released, which changed the texture of the precursor as the temperature was increased and finally the precursor decomposed to ACs, volatiles and gasses. The lower heating rates took more time to reach the final activation temperature 500 °C, which means the enduring of the precursor materials in a high heating atmosphere for a longer time. Thus, it had sufficient retention time to complete the pyrolysis process with the evolution of more volatiles and gasses, which increased the specific surface area and the mesopore volume. The activity of 50% H_3PO_4 followed the above trend for the aforementioned reason. However, the $ZnCl_2$ activation followed the opposite trend. In this regard, the surface area was increased with the increasing heating rate due to the breakage of the pore walls and blockage of the pores reacting with the inorganic acid HCl, which was generated by heating with 50% $ZnCl_2$ solution. Actually, the reaction mechanism and its efficiency on the minerals present within the precursor materials are different in case of acids or acidic salts at the same temperature increment rate. The pore size distribution curves provide evidence for the aforementioned statement. Fig. 2(c) and Fig. 2(d) clearly show that H10 had the highest pore volume among H10, HS10 and H30 when H_3PO_4 acid was the activating agent, and Zn30 had the highest pore volume among Zn10, Zn20 and Zn30 but lower than H10 when $ZnCl_2$ salt was the activating agent.

The surface functional groups of the ACs were examined by the Fourier-transform infrared spectrogram as shown in Fig. 4(a). The small peaks at 3,500-3,750 cm^{-1} may represent the O-H bond stretching of organics. It was observed that all the tested samples showed a small absorbance peak within the wave number 3,316-3,362 cm^{-1}. These peaks can be attributed to medium N-H bond stretching of aliphatic primary and secondary ammine groups. Small peaks were observed at 3,040-3,055 cm^{-1} and a broad diffused peak at 2,730-2,810 cm^{-1} due to C-H bond stretching of medium intensity in alkene and aldehydic groups respectively. C=O bond stretching of aliphatic ketone, carboxylic acid, conjugated acid, conjugated aldehyde or primary amide can be used to explain the formation of a slight peak at 1,690-1,711 cm^{-1}. Broad peaks were observed in the range 1,510-1,570 cm^{-1} either due to C=C stretching or due to N-O stretching. The peak at 1,250-1,275 cm^{-1} corresponds to the strong

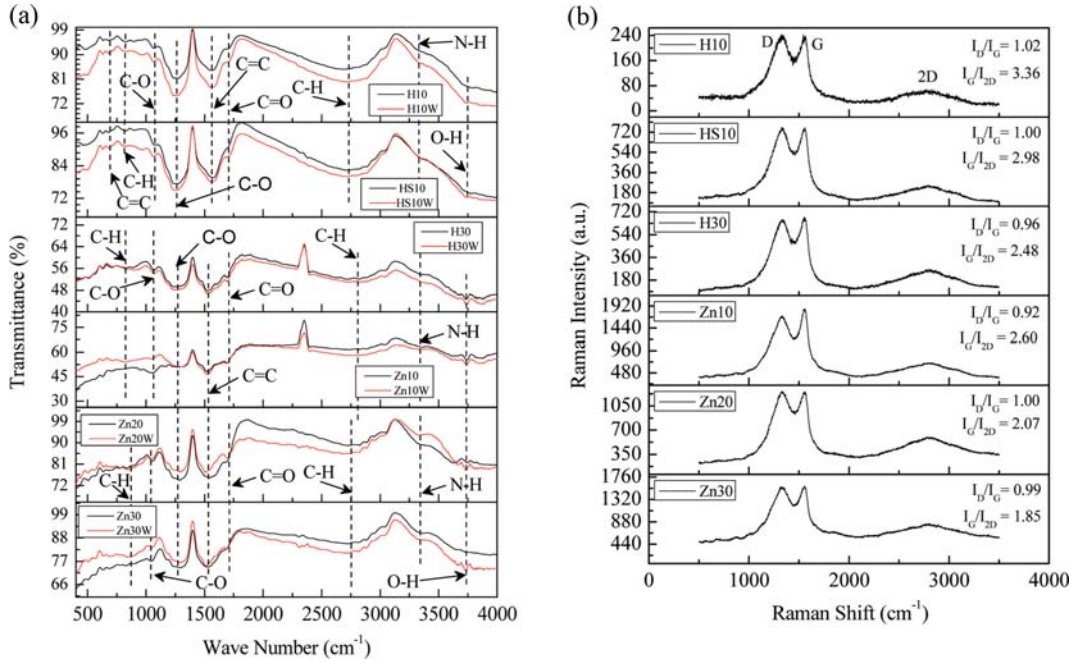

Fig. 4. Characterization of the AC (a) FTIR spectrograms and (b) Raman spectrograms.

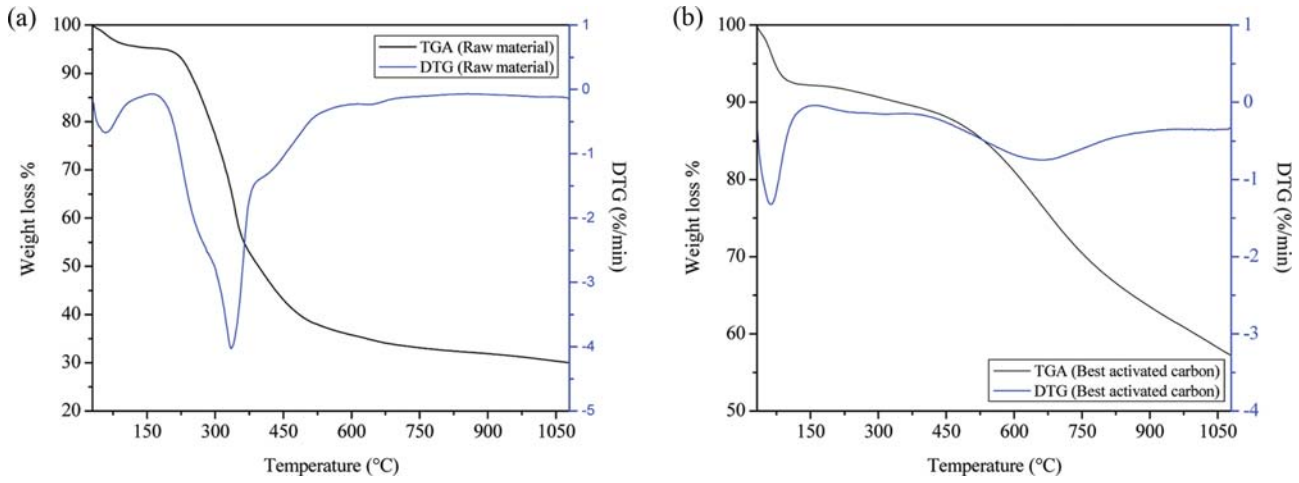

Fig. 5. Thermal (TG and DTG) analyses of (a) raw material and (b) best AC.

C-O bond stretching of aromatic ester or alkyl aryl ether. Strong C-O bond stretching for vinyl ether or primary alcohol can be used to interpret the peaks observed at 1,040-1,075 cm^{-1}. Bending of C=C alkene di-substituted (cis) bond was likely the cause of peaks observed at 684-706 cm^{-1} while strong bending of C-H bonds in 1,2,4-trisubstituted, 1,3-disubstituted, 1,4-disubstituted, 1,2,3,4-tetrasubstituted or mono-substituted Benzene derivative caused the peaks in 814-868 cm^{-1} [50-52,65]. All the ACs prepared by H_3PO_4 activation, characteristic bands at 980 cm^{-1} and 1,050 cm^{-1} correspond to P-O-P and P-O-C stretching, respectively. Whereas, the ACs prepared by $ZnCl_2$ activation, characteristic bands at 750 cm^{-1} and 876 cm^{-1} indicate the presence of C-Cl and OC-OH vibrational stretching [53]. The FTIR spectrogram demonstrated that the different heating rate does not change the functional groups. It depends mainly on the chemical composition of the precursor materials.

The presence of graphene layer or graphitic carbon in the prepared AC samples was analyzed by Raman spectroscopy to deduce the structure of the materials, particularly the presence of defects or disorders. Raman spectroscopy is highly sensitive to determine the morphology of the carbon materials. Each band in the Raman spectrogram corresponds to a particular vibrational frequency of a bond inside the molecule. The Raman spectrograms of the ACs as shown in Fig. 4(b), showed that the AC samples exhibit two significant peaks at 1,312-1,327 cm^{-1} (D-band) and 1,544-1,563 cm^{-1} (G-band) along with the 2D-band at 2,770-2,809 cm^{-1}. The graphitic peak (G band) at 1,542-1,558 cm^{-1} is due to the E_{2g} vibrational mode arising from the stretching of the C-C bond inside the graphitic materials, general to all sp^2 carbon systems. The disorder peak (D-band) at 1,312-1,327 cm^{-1} is significant for the A_{1g} vibrational mode arising from the disordered structure of sp^2-hybridized carbon systems. The intensity ratios (I_D/I_G) of 0.92-1.02 indicated the formation of the disordered graphitic carbon. All the AC materials exhibited a broad 2D-peak in the range of 2,770-2,809 cm^{-1} in the Raman spectra. The 2D-band along with the G-band in Raman spectrum is evidence of the graphitic sp^2 materials. The 2D-band is a second-order two-phonon process that exhibits a strong frequency dependence on the excitation laser energy. I_G/I_{2D} ratios greater than one is the proof of multilayer formation in the samples studied presently. Moreover, the I_G/I_{2D} ratios represent defect density in the synthesized carbon materials, with the increase of I_G/I_{2D} values the defect density increases [54]. In the present case that value decreases with the increase of heating rate, as with increasing heating rate providing less reaction time to the reactants, which results in less defect density. The best sample prepared according to BET surface area (H10) was the multilayered, amorphous and sp^2-hybridized graphitic carbon (I_D/I_G=1.02 and I_G/I_{2D}=3.36) as shown in Fig. 4(b).

Thermo-gravimetric analysis of the precursor materials showed that the mass of the materials were roughly constant after 500 °C, which helped to select the pyrolysis temperature of 500 °C (Fig. 5(a)). The samples were heated at 100 °C in an air oven for 24 hours before performing the TGA tests. Hence, the moisture content obtained from the TGA tests is only the bound moisture. The TGA and DTG plots of the best surface area AC clearly indicated the presence of three temperature zones in the activation process as shown in Fig. 5(b). The weight loss of 4.90% and 56.33% at the temperatures of 180 °C and 505 °C in Fig. 5(a) corresponds to the removal of water (dehydration) and the decomposition of the volatile components, respectively. The degradation of cellulose, hemi-cellulose and lignin from the precursor occurred in the temperature range of 180-505 °C [53,56]. Fig. 5(b) follows the same three thermal steps at relatively higher temperatures. The dehydration takes place at 186 °C and decomposition of cellulose, hemi-cellulose and lignin occurs at 540 °C with the weight loss of 7.94% and 7.35%, respectively [53]. The total weight loss was 42.58% at 1,080 °C. The DTG curves (Fig. 5(a) and 5(b)) represent the thermal energy released or absorbed per unit time during the decomposition process. The downward and upward movements of this curve represent the endothermic and the exothermic reactions, respectively. The AC is not completely degraded at 1,080 °C in the nitrogen atmosphere as shown in the TGA curve (Fig. 5(b)). Therefore, the prepared AC bears a high thermal stability in the inert atmosphere.

The FE-SEM image of H1OW (Fig. 6(a)), the pyrolyzed ACs without secondary activation, depicted the presence of porous (micropore and mesopore) irregular surface due to the effect of H_3PO_4 during the pyrolysis. Pyrolysis at 500 °C resulted in the cre-

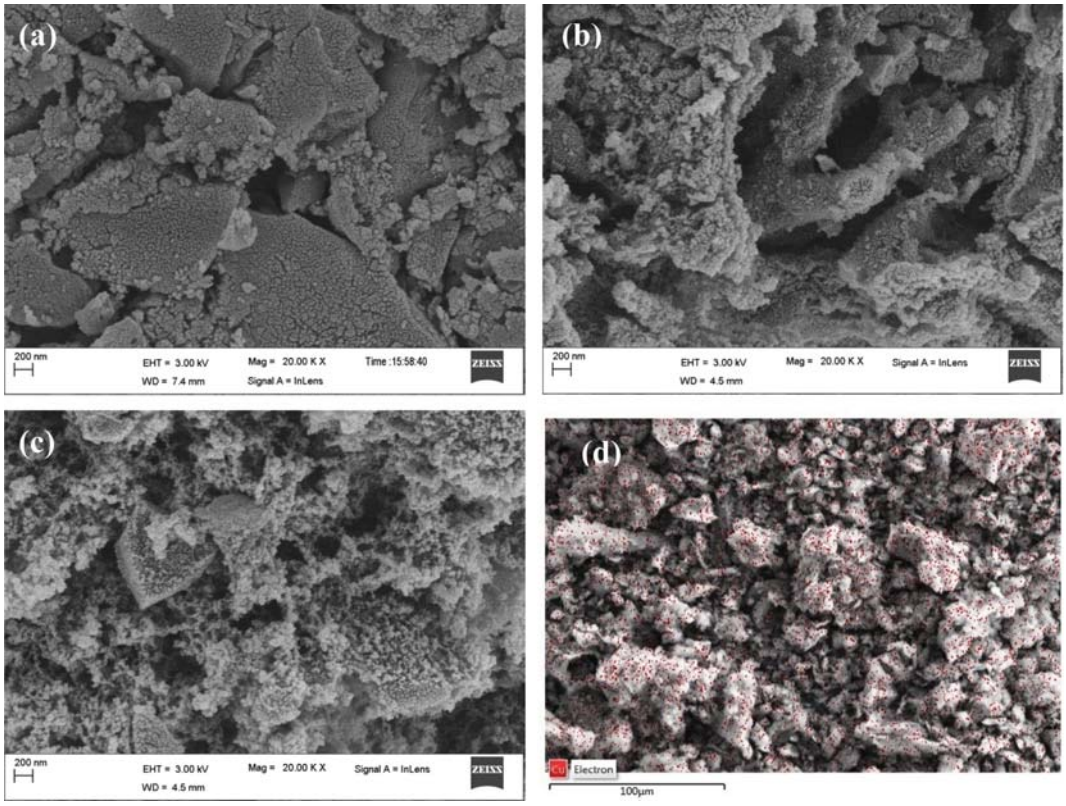

Fig. 6. Surface morphology (a) FE-SEM image of H10W, (b) FE-SEM image of H10, (c) FE-SEM image of H10 after copper (II) adsorption and (d) EDS mapping of H10 after copper (II) adsorption.

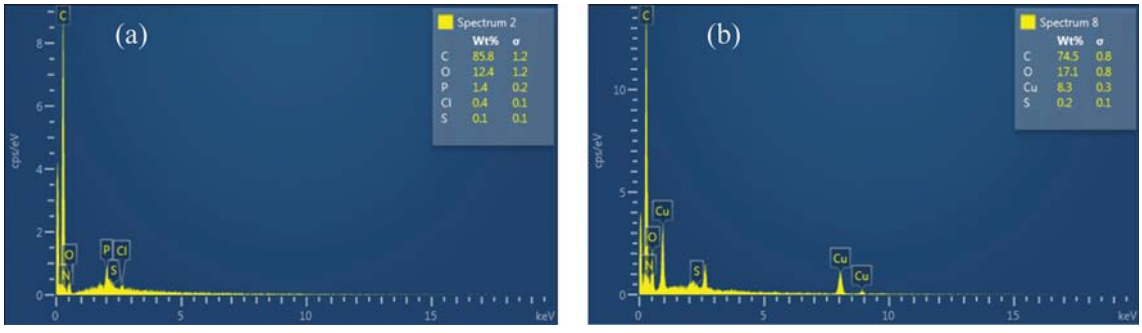

Fig. 7. EDS spectrum of (a) H10 and (b) H10 after copper adsorption.

ation of pores along with substantial removal of volatiles from the precursor. During the secondary activation or phosphate functionalization with pure 85% H_3PO_4 (1 : 2 ratio), the acid attacks the pore and increases the mesopore volume with the decrease of micropore volume. Well-developed pores were found on the surface of AC after the secondary activation (Fig. 6(b)). Fig. 6(c) represents the FE-SEM image of H10 after the copper (II) adsorption where the pores are blocked by the copper (II) metal ions. EDS mapping of the H10 after the copper (II) adsorption shown in Fig. 6(d) demonstrated that the copper (II) ions were adsorbed on the surface of the AC as represented by the red dots.

The fixed carbon and other compositions of the AC (H10) were analyzed by EDS composition analyzer, which are shown in Fig. 7(a), (b) and in Table 3. The copper (II) adsorption capacity of the AC (H10) can be inferred from Fig. 7(b), which holds the value of 83.00 mg/g. The actual value depending on the operating variables

Table 3. The elemental and proximate analysis of the best activated carbonprepared (H10)

Elemental analysis (wt%)		Proximate analysis (wt%)	
C	85.8	Moisture	12.94
H	2.26	Volatile matter	7.35
O	12.4	Ashes	4.93
N	4.7	Fixed carbon	74.76
S	0.1		
P	1.4		

is shown in section 3.2. The yield% of the AC (H10W) before washing was 85.24%. After the second activation, hot water washing and drying the yield% of the AC (H10) decreased to 42.36%.

2. Adsorption Analysis

2-1. Impact of the Initial pH on Adsorption

Experiments were carried out at three different pH values (2.42, 5.08 and 9.46) to understand the effect of initial pH on the Cu^{2+} adsorption process. These are the solution pH before the ACs addition, which will change a little after the carbon addition as the prepared AC (H10) bears a pH of 5.94. It was observed that the copper adsorption increased from 9.92 mg/g to 76.22 mg/g with the increased pH value from 2.42 to 9.46. The aqueous chemistry and the surface binding sites were both affected by the solution pH. The effect of solution pH on the copper adsorption processes is demonstrated in Fig. 8. The stiffness of each curve (Fig. 8) was decreased and gradually attained a constant value with the increased time, clearly indicating the rate of adsorption decreased with increasing time due to the occupancy of the vacant sites on the adsorbent with the adsorbate molecules. With decreasing pH value, the number of H^+ ions in the solution increased. The adsorbate molecules (Cu^{2+}) competed with the H^+ ions (ionic radius=53 picometer) to occupy the vacant sites, and hence the copper adsorption decreased as the surface behaved as positively charged occupied by the H^+ ions. With the increased pH value, the number of OH^- ions (ionic radius=110 picometer) in the solution increased and the copper adsorption increased as the movement of Cu^{2+} ions (ionic radius=73 picometer [66]) towards the adsorbent, which dominated the movement of OH^- and NH_4^+ (ionic radius=152 picometer [66]) ions. Some OH^- ions along with PO_4^- bonded with the surface functional groups of the adsorbent, resulting in the negatively charged surface, increased the copper adsorption in the basic range [34,55]. On the other hand, with the increase of pH values, the solubility of the copper ions in the aqueous phase decreased, which resulted in higher adsorption

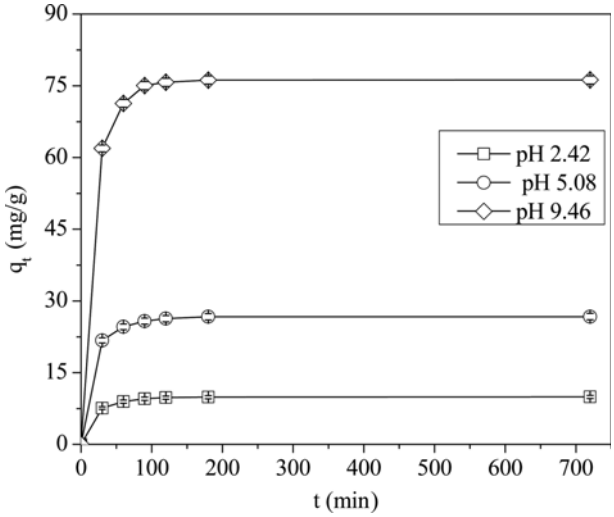

Fig. 8. Effect of pH and time on the copper adsorption.

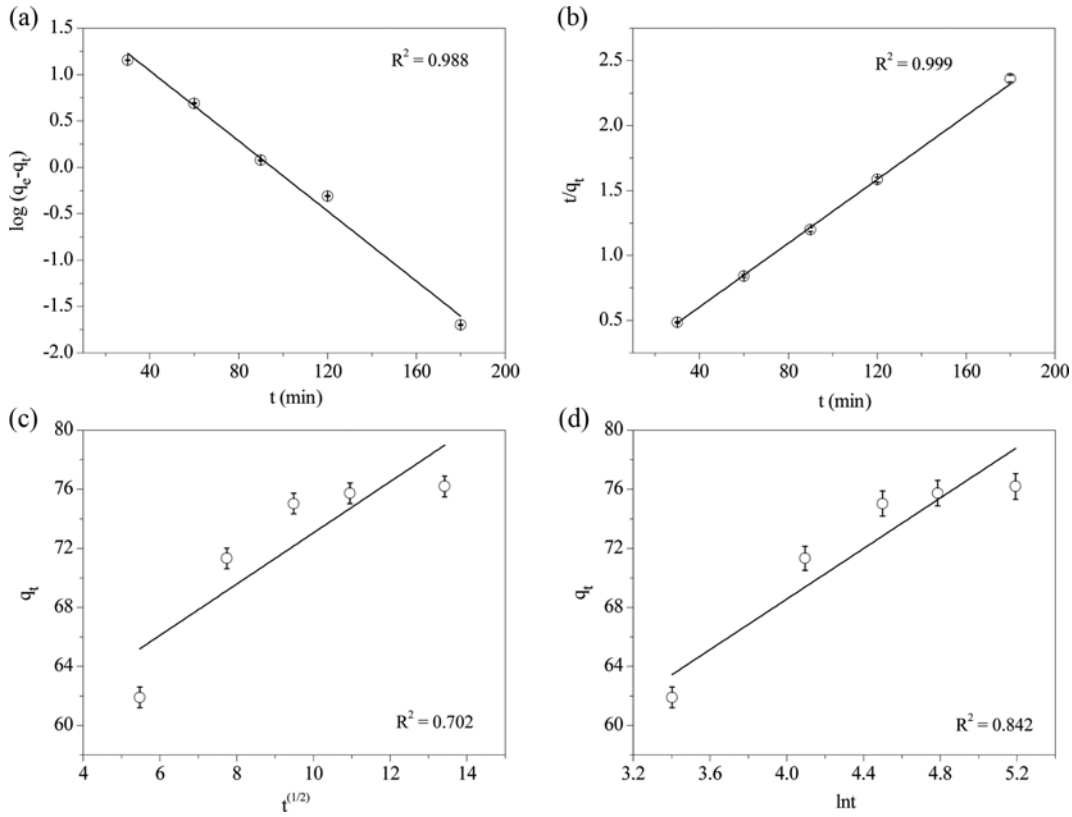

Fig. 9. Copper adsorption kinetics: (a) Pseudo-first-order model, (b) Pseudo-second-order model, (c) Intraparticle diffusion model and (d) Elovich model.

initially. At pH values higher than the prior, positively charged copper amine complex ($Cu(NH_3)_4^{2+}$) formed, which facilitated its adsorption on the negatively charged AC surfaces.

2-2. Adsorption Kinetics

Four kinetic models--pseudo-first-order, pseudo-second-order, intraparticle diffusion and Elovich--were used to determine the controlling mechanism of the Cu^{2+} sorption process. Pseudo-first-order model in the linearized form can be expressed as [37]:

$$\log(q_e - q_t) = \log q_e - \frac{k_1 t}{2.303} \quad (1)$$

The amount of copper (II) adsorbed (mg/g) on the AC at equilibrium and at time t are represented by q_e and q_t, respectively. The parameter, k_1 is the first-order rate constant. The values of k_1 were obtained from the $\log(q_e - q_t)$ versus t (min) plot for the variant concentration of Cu^{2+} ions (Fig. 9(a)). The pseudo-second-order kinetic model can be represented by [38,56,57]:

$$\frac{t}{q_t} = \frac{1}{k_2 q_e^2} + \frac{t}{q_e} \quad (2)$$

where k_2 is the second-order rate constant (g/mg min). The values of k_2 and q_e can be calculated from the intercept and slope of the plot of t/q_t against t (Fig. 9(b)). A model calculation of pseudo-second-order kinetics is shown in Table S2. The intraparticle diffusion equation is represented by [37,56]:

$$q_t = k_p t^{1/2} + C \quad (3)$$

where C is the intercept and k_p is the rate constant (mg/g $min^{1/2}$) of the intra-particle kinetic model, which is obtained from the slope of q_t versus $t^{1/2}$ plot (Fig. 9(c)). This model is used to understand the steps of the diffusion. The Elovich kinetic model is used to examine the presence of chemical adsorption processes which is applicable for the heterogeneous absorbing surfaces. The linearized form of the Elovich equation is [58]:

$$q_t = \frac{\ln(a_e b_e)}{b_e} + \frac{1}{b_e}\ln t \quad (4)$$

where a_e and b_e are the initial sorption rate (mg/g min) and the scope of surface coverage for the chemisorption (g/mg), which are obtained from the intercept and slope of the q_t versus lnt plot (Fig. 9(d)). The average relative errors (ARE%) were calculated by using Eq. (5) to find a suitable match for the experimental data with the kinetic and isotherm models.

$$ARE(\%) = \frac{100}{N}\sum_{1}^{N}\left|\frac{q_{cal} - q_{exp}}{q_{exp}}\right| \quad (5)$$

where N represents the number of data points. q_{exp} and q_{cal} (mg/g) are the equilibrium values obtained from the experiment and the isotherm model, respectively. The parameters of the kinetic models are shown in Table 4. The pseudo-second-order model was best fitted with the experimental data with the correlation coefficient of R^2=0.999 and the low ARE% of 3.62. The calculated q_e (79.68 mg/g) was closer to the experimental value (76.22 mg/g), indicating best suited pseudo-second-order model. Despite the low correlation coefficient value (R^2=0.842), the Elovich model showed lower ARE% of 2.36, which was also evidence of chemical adsorption. Hence, the predominant process in the present study is chemisorption as reported earlier [35,59].

Table 4. Kinetic parameters for Cu^{2+} adsorption onto the AC (Cu^{2+} concentration: 92.55 mg/*l*, 50 ml Cu^{2+} solution, 0.05 g AC, pH: 9.46, temperature: 301 K and contact time: 30-270 min)

Kinetic models	Kinetic parameters		R^2	ARE%
Pseudo-first-order	k_1=0.0435	q_e=62.65	0.988	19.78
Pseudo-second-order	k_2=0.0018	q_e=79.68	0.999	3.62
Intraparticle diffusion	k_p=1.7016	C=56.07	0.702	3.33
Elovich	a_e=801.95	b_e=0.1248	0.842	2.36

2-3. Adsorption Isotherms

Four adsorption isotherm models, Langmuir, Freundlich, Temkin and Dubinin-Radushkevich (D-R), were studied in the present context. The Langmuir adsorption model, which is applicable for many monolayer adsorption processes, can be represented as [35]:

$$\frac{C_e}{q_e} = \frac{1}{bQ_m} + \frac{C_e}{Q_m} \quad (6)$$

where C_e and q_e are the solution concentration of Cu^{2+} at equilibrium (mg/*l*) and the amount of copper adsorbed on the AC (mg/g), respectively. The calculations related to Langmuir isotherm are documented in Table S3. The adsorption equilibrium constant is represented as b (*l*/mg) and Q_m is the maximum adsorption capacity (mg/g). The adsorption coefficients were determined from the intercept and slope of a plot of C_e/q_e versus C_e (Fig. 10(a)). The heterogeneous systems are described by an empirical equation called Freundlich isotherm, which is expressed as [38]:

$$\log q_e = \log k_f + \frac{1}{n}\log C_e \quad (7)$$

The adsorption capacity and its intensity are represented by the terms k_f and n, which were determined from the intercept and slope of $\log q_e$ versus $\log C_e$ plot (Fig. 10(b)). The Temkin isotherm model accounts for the adsorbate and adsorbent interaction. The heat of adsorption decreasing linearly with the coverage and the uniform distribution of binding energy are the main assumptions of this model. The Temkin adsorption isotherm model can be represented as [60]:

$$q_e = B\ln k_t + B\ln C_e \quad (8)$$

The Temkin adsorption isotherm constants k_t (equilibrium binding energy, *l*/mg) and B (related to the heat of sorption) were calculated from the q_e versus $\ln C_e$ plot (Fig. 10(c)). D-R model is generally used to analyze the sorption processes where the surface is heterogeneous and the sorption potentials of the sorption sites are variable. The linear form of D-R model is expressed as [61]:

$$\ln q_e = \ln q_s - B'\varepsilon^2 \quad (9)$$

where ε is the Polanyi potential, related to the equilibrium as follows:

$$\varepsilon = RT\ln\left(1 + \frac{1}{C_e}\right) \quad (10)$$

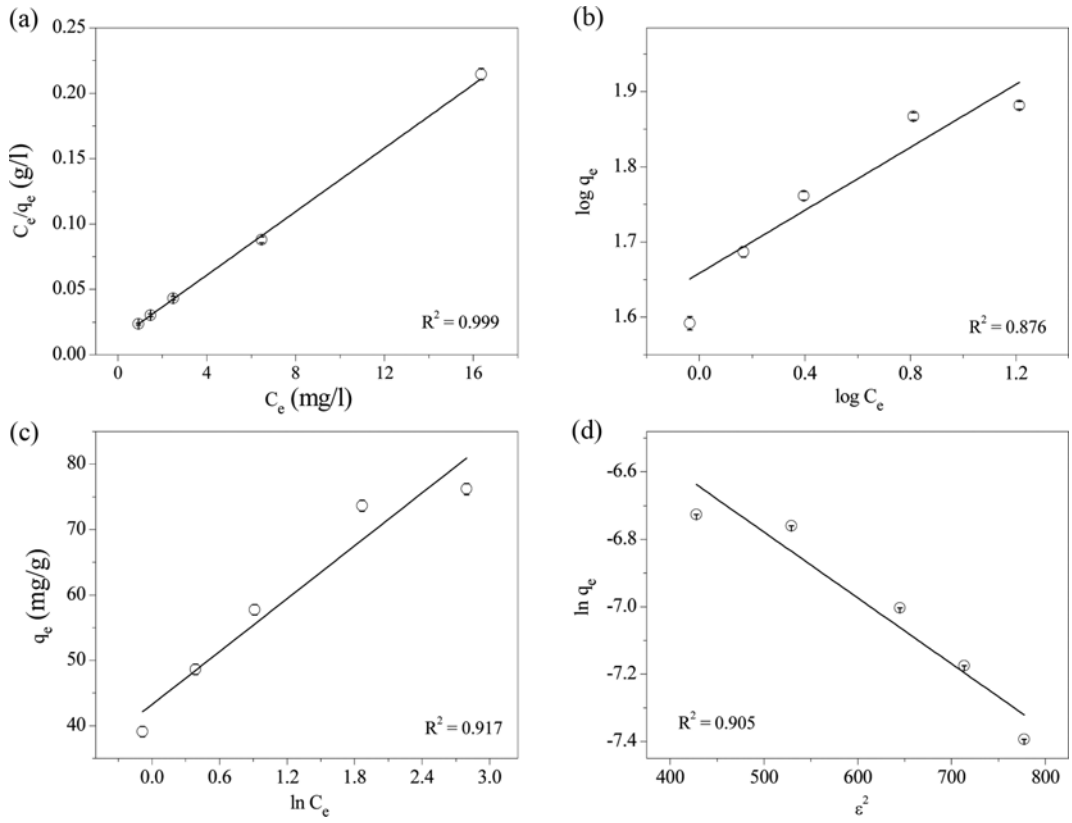

Fig. 10. Adsorption isotherm models: (a) Langmuir, (b) Freundlich, (c) Temkin and (d) Dubinin-Radushkevich (D-R).

In Eq. (9), q_s and q_e are the adsorption capacity (mol/g) and the concentration of copper (II) in equilibrium on the adsorbent surface (mol/g), respectively. The model constants q_s and B' (mol^2/kJ^2) are obtained from the $\ln q_e$ versus ε^2 plot (Fig. 10(d)). C_e is the solution concentration of Cu^{2+} at equilibrium (mol/*l*), R is the universal gas constant (8.314×10^{-3} kJ/mol K) and T (K) is the absolute temperature (Eq. (10)). The mean free energy of adsorption (E) is obtained by Eq. (11), which is calculated with the aforementioned B′ value [62].

$$E = 1/\sqrt{2B'} \quad (11)$$

When the E value lies within 8-16 kJ/mol, chemical adsorption occurs, whereas the value below 8 kJ/mol facilitates the physical adsorption process [63]. In the present study, the E value at the pH value of 9.46 was found to be 16.09 kJ/mol, corresponding to the chemical adsorption process. The isotherm models are shown in Fig. 10, and the constants of the models are tabulated in Table 5. The calculations of D-R model are shown in Table S4. The Langmuir isotherm model satisfies our experimental data significantly well with the correlation coefficient of 0.999 and ARE% of 2.41. The Langmuir monolayer adsorption capacity was 80.91 mg/g, which is very near to our experimental data 76.22 mg/g. The constant k_f, in the Freundlich adsorption isotherm shows the propensity of the adsorbent to adsorb, and n represents the capability of the adsorbate to be adsorbed. The n value greater than 1 proved the favorable sorption of Cu^{2+} onto the prepared AC.

Table 5. Cu^{2+} adsorption constants onto the AC (Cu^{2+} concentration: 40.02, 50.08, 60.23, 80.12 and 92.55 mg/*l*, 50 ml Cu^{2+} solution, 0.05 g AC, pH: 9.46, temperature: 301 K and contact time: 720 min)

Isotherms	Temperature (K)	Constants		R^2	ARE%
Langmuir	301	Q_m=80.91	b=1.08	0.999	2.41
Freundlich	301	k_f=43.62	n=4.32	0.876	1.77
Temkin	301	B=13.31	K_t=26.06	0.917	5.05
D-R	301	q_s=0.0029	B′=0.0019	0.905	6.34

As stated by the previous explanation, the sorption of Cu^{2+} onto the AC follows Langmuir and D-R type of sorption models. The Langmuir adsorption model explains the monolayer formation of the Cu (II) on the identical and energetically equivalent (homogeneous) sites of the AC (adsorbent). D-R isotherm provides the overall heterogeneous solid surfaces. The surface of the prepared AC in the present study consists of small heterogeneous adsorption sites (Fig. 6(b)), similar to the sorption phenomena by Ahmad et al. [64]. Note that the best AC prepared from the tea waste may be used as a promising Cu (II) adsorbent with the highest adsorption capacity (76.22 mg/g) reported so far.

CONCLUSIONS

The best surface area (1,329 m^2/g) AC was prepared from the tea waste following a three-step activation process by H_3PO_4 acti-

vation providing the significance of secondary activation or phosphate functionalization. The pseudo-second-order kinetic model was followed by the adsorption process quite satisfactorily (R^2=0.999) with the ARE% 3.62. The adsorption of Cu^{2+} ions onto the AC was adequately supported by the Langmuir and D-R adsorption models with the maximum adsorption capacity of 76.22 mg/g at a pH value of 9.46 and at 28 °C. The AC synthesized from the tea waste may be utilized as a potential adsorbent for the significant removal of Cu^{2+} from basic solutions.

ACKNOWLEDGEMENTS

The authors are grateful to Analytical laboratory, department of Chemical Engineering and Central Instrument Facility, Indian Institute of Technology Guwahati for the assistance and support to perform the necessary analysis. The authors would like to thank Mr. Saptarshi Sengupta, Jadavpur University, for his initial help during the ACs preparation.

NOMENCLATURE

a_e : initial adsorption rate of Elovich equation [mg/g min]
b : Langmuir's equilibrium constant [*l*/mg]
B : Temkin adsorption isotherm constant (related to the heat of adsorption)
B' : Dubinin-Radushkevich (D-R) model constant [mol^2/kJ^2]
b_e : extent of surface coverage for chemisorption in Elovich equation [g/mg]
C_0 : initial metal ion concentration in solution [mg/*l*]
C_e : solution concentration at equilibrium [mg/*l* or mol/g]
E : mean free energy of adsorption [kJ/mol]
k_1 : pseudo first-order rate constant [1/min]
k_2 : pseudo second-order rate constant [g/mg min]
k_f : Freundlich's constant [related to adsorption capacity, $mg^{1-1/n}$ $l^{1/n}$/g]
k_p : rate constant of the intraparticle diffusion model [mg/g $min^{1/2}$]
k_t : Temkin adsorption isotherm constant [equilibrium binding energy, *l*/mg]
n : Freundlich's constant [related to adsorption intensity, -]
N : number of data points [-]
q_{cal} : equilibrium values obtained from the isotherm model [mg/g]
q_e : adsorption capacity at equilibrium [mg/g or mol/g]
q_{exp} : equilibrium values obtained from the experiment [mg/g]
Q_m : maximum adsorption capacity [mg/g]
q_s : Dubinin-Radushkevich (D-R) model constant or adsorption capacity [mol/g]
q_t : adsorption capacity at time t [mg/g]
R : universal gas constant [kJ/mol K]
T : temperature [K]
t : time [min]
ε : Polanyi potential [-]

SUPPORTING INFORMATION

Additional information as noted in the text. This information is available via the Internet at http://www.springer.com/chemistry/journal/11814.

REFERENCES

1. M. Ahmaruzzaman and S. L. Gayatri, *J. Chem. Eng. Data*, **55**, 4614 (2010).
2. B. Tiryaki, E. Yagmur, A. Banford and Z. Aktas, *J. Anal. Appl. Pyrolysis*, **105**, 276 (2014).
3. Y. Gokce and Z. Aktas, *Appl. Surf. Sci.*, **313**, 352 (2014).
4. I. I. G. Inal, S. M. Holmes, A. Banford and Z. Aktas, *Appl. Surf. Sci.*, **357**, 696 (2015).
5. M. Goswami and P. Phukan, *J. Environ. Chem. Eng.*, **5**, 3508 (2017).
6. Y. Kan, Q. Yue, D. Li, Y. Wu and B. Gao, *J. Taiwan Inst. Chem. E.*, **71**, 494 (2017).
7. E. Yagmur, S. Turkoglu, A. Banford and Z. Aktas, *J. Clean. Prod.*, **149**, 1109 (2017).
8. S. Wong, Y. Lee, N. Ngadi, I. M. Inuwa and N. B. Mohamed, *Chinese J. Chem. Eng.*, **26**, 1003 (2018).
9. E. Akar, A. Altinis and Y. Seki, *Ecol. Eng.*, **52**, 19 (2013).
10. M. A. Islam, A. Benhouria, M. Asif and B. H. Hameed, *J. Taiwan Inst. Chem. E.*, **52**, 57 (2015).
11. M. Auta, *Int. J. Adv. Res. Technol.*, **I**(IV), 50 (2012).
12. R. Menon, J. Singh, V. Doshi and X. Y. Lim, *J. Eng. Sci. Technol.*, **Special Issue**, 50 (2015).
13. C. Peng, X. B. Yan, R. T. Wang, J. W. Lang, Y. J. Ou and Q. J. Xue, *Electrochim. Acta*, **87**, 401 (2013).
14. S. DeokSeo, C. Choi, B. Kook Kim and D. Wan Kim, *Ceram. Int.*, **43**, 2836 (2017).
15. A. Gundogdu, C. Duran, H. B. Senturk, M. Soylak, M. Imamoglu and Y. Onal, *J. Anal. Appl. Pyrolysis*, **104**, 249 (2013).
16. P. A. Chen, H. C. Cheng and H. P. Wang, *J. Clean. Prod.*, **174**, 927 (2018).
17. M. Auta and B. H. Hameed, *Chem. Eng. J.*, **175**, 233 (2011).
18. C. Duran, D. Ozdes, A. Gundogdu, M. Imamoglu and H. B. Senturk, *Anal. Chim. Acta*, **688**, 75 (2011).
19. M. Auta and B. H. Hameed, *Chem. Eng. J.*, **171**, 502 (2011).
20. P. Kalyani and A. Anitha, *Port. Electrochim. Acta*, **31**, 165 (2013).
21. L. Borah, M. Goswami and P. Phukan, *J. Environ. Chem. Eng.*, **3**, 1018 (2015).
22. Z. N. Garba, S. F. B. Soib and A. A. Rahim, *J. Chem. Eng. Chem. Res.*, **2**, 623 (2015).
23. S. Fan, Y. Wang, J. Tang, H. Li, H. Zhang, J. Tang, Z. Wang and X. Li, *J. Mol. Liq.*, **220**, 432 (2016).
24. A. H. P. Hettiarachchi and C. S. K. Rajapakse, *J. Chem. Sci.*, **8**, 7 (2018).
25. A. Zuorro, M. L. Santarelli and R. Lavecchia, *Adv. Mater. Res.*, **803**, 26 (2013).
26. K. M. Rani, P. N. Palanisamy, S. Gayathri and S. Tamilselvi, *Int. J. Innov. Res. Sci. Eng. Technol.*, **4**, 6845 (2015).
27. M. Vithanage, S. S. Mayakaduwa, I. Herath and Y. S. Ok, *Chemosphere*, **150**, 781 (2016).
28. A. Gundogdu, C. Duran, H. B. Senturk, M. Soylak, D. Ozdes, H. Serencam and M. Imamoglu, *J. Chem. Eng. Data*, **57**, 2733 (2012).
29. A. U. Rajapaksha, M. Vithanage, M. Zhang, M. Ahmad, D. Mohan, S. X. Chang and Y. S. Ok, *Bioresour. Technol.*, **166**, 303 (2014).

30. M. Dutta, U. Das, S. Mondal, S. Bhattachriya, R. Khatun and R. Bagal, *Int. J. Environ. Sci.*, **6**, 270 (2015).
31. J. Li, G. Yu, L. Pan, C. Li, F. You, S. Xie, Y. Wang, J. Ma and X. Shang, *J. Environ. Sci.*, **73**, 20 (2018).
32. L. Borah, K. K. Senapati, C. Borgohain, S. Sarma, S. Roy and P. Phukan, *J. Porous Mat.*, **19**, 1 (2011).
33. U. A. Isah and M. Lawal, *Adv. Appl. Sci. Res.*, **3**, 4033 (2012).
34. X. Wang, X. Liang, Y. Wang, X. Wang, M. Liu, D. Yin, S. Xia, J. Zhao and Y. Zhang, *Desalination*, **278**, 231 (2011).
35. E. Demirbas, N. Dizge, M. T. Sulak and M. Kobya, *Chem. Eng. J.*, **148**, 480 (2009).
36. J. C. M. Pirajan and L. Giraldo, *J. Anal. Appl. Pyrolysis*, **87**, 188 (2010).
37. F. Bouhamed, Z. Elouear and J. Bouzid, *J. Taiwan Inst. Chem. E.*, **43**, 741 (2012).
38. H. Demiral and C. Gungor, *J. Clean. Prod.*, **124**, 103 (2016).
39. M. O. A. Badmus, T. O. K. Audu and B. Anyata, *Korean J. Chem. Eng.*, **24**, 246 (2007).
40. E. Sayan, *Chem. Eng. J.*, **115**, 213 (2006).
41. M. H. Kalavathy, T. Karthikeyan, S. Rajgopal and L. R. Miranda, *J. Colloid Interface Sci.*, **292**, 354 (2005).
42. K. Periasamy and C. Namasivayam, *Chemosphere*, **32**, 769 (1996).
43. C. Namasivayam and K. Kadirvelu, *Chemosphere*, **34**, 377 (1997).
44. M. M. Rao, A. Ramesh, G. P. C. Rao and K. Seshaiah, *J. Hazard. Mater.*, **B129**, 123 (2006).
45. J. Du, L. Liu, L. Zhang, Y. Yu, Y. Zhang and A. Chen, *J. Renew. Sustain. Energy*, **9**, 1 (2017).
46. Z. Hu, M. P. Srinivasan and Y. Ni, *Carbon*, **39**, 877 (2001).
47. R. C. Bansal and M. Goyal, Activated Carbon Adsorption, Taylor and Francis Group, CRC Press, Boca Raton, FL (2005).
48. L. Tang, J. Yu, Y. Pang, G. Zeng, Y. Deng, J. Wang, Y. Liu, H. Feng, S. Chen and X. Ren, *Chem. Eng. J.*, **336**, 160 (2018).
49. J. Yu, L. Tang, Y. Pang, G. Zeng, J. Wang, Y. Deng and Z. Zheng, *Chem. Eng. J.*, **364**, 146 (2019).
50. T. Budinova, E. Ekinci, F. Yardim, A. Grimm, E. Bjornbom and V. Minkova, *Fuel Process. Technol.*, **87**, 899 (2006).
51. Z. Wang, E. Nie, J. Li, M. Yang, Y. Zhao, X. Luo and Z. Zheng, *Environ. Sci. Pollut. Res.*, **19**, 2908 (2012).
52. Y. Li, H. Jin, W. Liu, H. Su, Y. Lu and J. Li, *Sci. Rep.*, **8**, 1 (2018).
53. M. Danish, R. Hashim, M. N. M. Ibrahim and O. J. Sulaiman, *Anal. Appl. Pyrolysis*, **104**, 418 (2013).
54. Z. Luo, T. Yu, Z. Ni, S. Lim, H. Hu, J. Shang, L. Liu, Z. Shen and J. Lin, *J. Phys. Chem. C*, **115**, 1422 (2011).
55. Y. Liu, X. Liu, W. Dong, L. Zhang, Q. Kong and W. Wang, *Sci. Rep.*, **7**, 1 (2017).
56. A. Ozcan, A. S. Ozcan, S. Tunali, T. Akar and I. Kiran, *J. Hazard. Mater.*, **B124**, 200 (2005).
57. Sandy, V. Maramis, A. Kurniawan, A. Ayucitra, J. Sunarso and S. Ismadji, *Front. Chem. Sci. Eng.*, **6**, 58 (2012).
58. P. L. Homagai, K. N. Ghimire and K. Inoue, *Bioresour. Technol.*, **101**, 2067 (2010).
59. X. Gao, L. Wu, Q. Xu, W. Tian, Z. Li and N. Kobayashi, *Environ. Sci. Pollut. Res. Int.*, **25**, 7907 (2018).
60. Z. Cheng, L. Zhang, X. Guo, X. Jiang and T. Li, *Spectrochim. Acta A Mol. Biomol. Spectroscopy*, **137**, 1126 (2015).
61. M. Ghaedi, A. Ansari, M. H. Habibi and A. R. Asghari, *J. Ind. Eng. Chem.*, **20**, 17 (2014).
62. P. G. Gonzalez and Y. B. Pliego-Cuervo, *Chem. Eng. Res. Des.*, **92**, 2715 (2014).
63. T. E. Kose, H. Demiral and N. Oztürk, *Desalin. Water Treat.*, **29**, 110 (2011).
64. A. Ahmad, M. Rafatullah, O. Sulaiman, M. H. Ibrahim, Y. Y. Chii and B. M. Siddique, *Desalination*, **247**, 636 (2009).
65. Infrared spectroscopy adsorption table, chemistry, LibreTexts™ https://chem.libretexts.org/Reference/Reference_Tables/Spectroscopic_Parameters/Infrared_Spectroscopy_Absorption_Table.
66. Sizes of Atoms and Ions, LibreTexts™https://chem.libretexts.org/Bookshelves/General_Chemistry/Map%3A_Chemistry_-_The_Central_Science_(Brown_et_al.)/07._Periodic_Properties_of_the_Elements/7.3%3A_Sizes_of_Atoms_and_Ions.